

Shallow particulate organic carbon regeneration in the South Pacific Ocean

Frank J. Pavia^{a,b,1}, Robert F. Anderson^{a,b}, Phoebe J. Lam^c, B. B. Cael^{d,e}, Sebastian M. Vivancos^{a,b}, Martin Q. Fleisher^b, Yanbin Lu^f, Pu Zhang^f, Hai Cheng^{f,g}, and R. Lawrence Edwards^f

^aLamont-Doherty Earth Observatory, Columbia University, Palisades, NY 10964; ^bDepartment of Earth and Environmental Sciences, Columbia University, New York, NY 10027; ^cDepartment of Ocean Sciences, University of California, Santa Cruz, CA 95064; ^dDaniel K. Inouye Center for Microbial Oceanography: Research and Education, University of Hawai'i at Mānoa, Honolulu, HI 96822; ^eDepartment of Oceanography, School of Ocean and Earth Science and Technology, University of Hawai'i at Mānoa, Honolulu, HI 96822; ^fDepartment of Earth Sciences, University of Minnesota, Minneapolis, MN 55455; and ^gInstitute of Global Environmental Change, Xi'an Jiaotong University, Xi'an 710054, China

Edited by David M. Karl, University of Hawaii, Honolulu, HI, and approved April 8, 2019 (received for review January 31, 2019)

Particulate organic carbon (POC) produced in the surface ocean sinks through the water column and is respired at depth, acting as a primary vector sequestering carbon in the abyssal ocean. Atmospheric carbon dioxide levels are sensitive to the length (depth) scale over which respiration converts POC back to inorganic carbon, because shallower waters exchange with the atmosphere more rapidly than deeper ones. However, estimates of this carbon regeneration length scale and its spatiotemporal variability are limited, hindering the ability to characterize its sensitivity to environmental conditions. Here, we present a zonal section of POC fluxes at high vertical and spatial resolution from the GEOTRACES GP16 transect in the eastern tropical South Pacific, based on normalization to the radiogenic thorium isotope ^{230}Th . We find shallower carbon regeneration length scales than previous estimates for the oligotrophic South Pacific gyre, indicating less efficient carbon transfer to the deep ocean. Carbon regeneration is strongly inhibited within suboxic waters near the Peru coast. Canonical Martin curve power laws inadequately capture POC flux profiles at suboxic stations. We instead fit these profiles using an exponential function with flux preserved at depth, finding shallow regeneration but high POC sequestration below 1,000 m. Both regeneration length scales and POC flux at depth closely track the depths at which oxygen concentrations approach zero. Our findings imply that climate warming will result in reduced ocean carbon storage due to expanding oligotrophic gyres, but opposing effects on ocean carbon storage from expanding suboxic waters will require modeling and future work to disentangle.

biological pump | ocean carbon storage | oxygen-deficient zones | GEOTRACES | thorium

The oceanic biological pump encompasses a series of processes by which phytoplankton at the sea surface photosynthetically fix carbon dioxide (CO_2) to form particulate organic carbon (POC), a portion of which is exported from the upper ocean and sinks to depth, where it is regenerated by microbial respiration (1, 2). The first two components of the biological pump, primary production and export of POC from the upper ocean, have been sufficiently characterized to enable their parametrization in terms of variables that can be measured by satellites, allowing for comprehensive estimates of their global rates and spatiotemporal variability (3–6). However, the fate of exported POC upon sinking into the ocean interior has proved to be an elusive oceanographic target. Because the time scale that waters are sequestered from the atmosphere increases with depth, the length scale over which POC regeneration occurs exerts a strong control on oceanic carbon storage and atmospheric CO_2 levels (7). Consequently, assessing how environmental conditions influence POC regeneration length scales provides critical insights that can be incorporated into ocean carbon cycle models to improve projections of future oceanic CO_2 uptake, including the response to global warming.

Historical estimates of carbon regeneration in the ocean interior have come from POC flux profiles generated either by compilations of sediment traps (8); by individual free-floating sediment trap profiles, typically with three to six depths in the upper 500 m (9, 10); or by combining ^{234}Th -based euphotic zone POC fluxes with those from bottom-moored sediment traps below 1,500 m (11, 12). POC regeneration length scales are then determined by fitting either power laws (8) or exponential functions (13) to the vertical profiles of POC flux. However, these methods are respectively limited by their spatial resolution, vertical resolution, and integration across different temporal and spatial domains. The methods also provide conflicting results on the spatial patterns of regeneration depths, precluding the development of a comprehensive mechanistic understanding of the processes that control POC regeneration (9, 11).

We determine POC regeneration length scales in the eastern tropical South Pacific by adapting the paleoceanographic ^{230}Th -normalization method (14) to the water column. Our study is the first application of this approach to generate internally consistent, high-resolution POC flux profiles that resolve differences in POC flux characteristics across biogeochemical gradients on annual to multiannual time scales. By analyzing particulate ^{230}Th ($^{230}\text{Th}_p$) and POC collected by in situ filtration, we calculate POC fluxes, integrated across ~1- to 3-y time scales, at each measurement depth (15, 16) (see *Materials and Methods*). A

Significance

Plankton in the sunlit surface ocean photosynthesize, fixing dissolved CO_2 into particulate organic carbon (POC). This POC sinks and is respired, releasing CO_2 into subsurface waters that are sequestered from the atmosphere. The depth scale over which this regeneration happens strongly affects atmospheric CO_2 , but estimates to date have been sparse and challenging to interpret. We use a new geochemical method to determine POC regeneration depth scales at unprecedented resolution in the South Pacific Ocean, finding shallow regeneration in both oxygen-deficient zone and oligotrophic gyre settings. Our results imply decreased future ocean carbon storage due to gyre expansion and two opposing feedbacks to expanding oxygen-deficient zones, the net effects of which on ocean carbon storage require future research.

Author contributions: F.J.P., R.F.A., P.J.L., and R.L.E. designed research; F.J.P., B.B.C., S.M.V., M.Q.F., Y.L., P.Z., and H.C. performed research; F.J.P., B.B.C., M.Q.F., and P.Z. analyzed data; and F.J.P. wrote the paper with input from R.F.A., P.J.L., and B.B.C.

The authors declare no conflict of interest.

This article is a PNAS Direct Submission.

Published under the PNAS license.

¹To whom correspondence should be addressed. Email: fpavia@ldeo.columbia.edu.

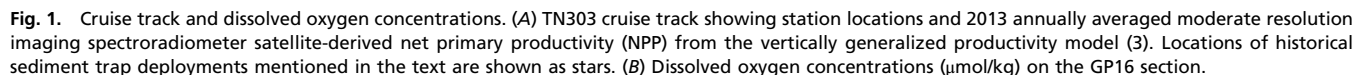
This article contains supporting information online at www.pnas.org/lookup/suppl/doi:10.1073/pnas.1901863116/-DCSupplemental.

PNAS

Results and Discussion

Regeneration length scales are traditionally expressed using a power law relationship (8). We fit power laws of form

$F_z = F_{z_0} \left(\frac{z}{z_0} \right)^{-b}$ to POC fluxes in the upper 1,000 m at each station to predict the POC flux (F_z) at depth z , relative to a reference depth z_0 , with the exponent b describing the rate of flux attenuation with depth. Stations 15 to 36, west of the Peru upwelling region, have average b values of 1.29 ± 0.12 (Fig. 3), much higher (i.e., shallower, faster regeneration) than previous estimates for the SPSS derived from the combination of bottom-moored sediment traps and ^{234}Th ($b = 0.52$) (11, 12) and a follow-up



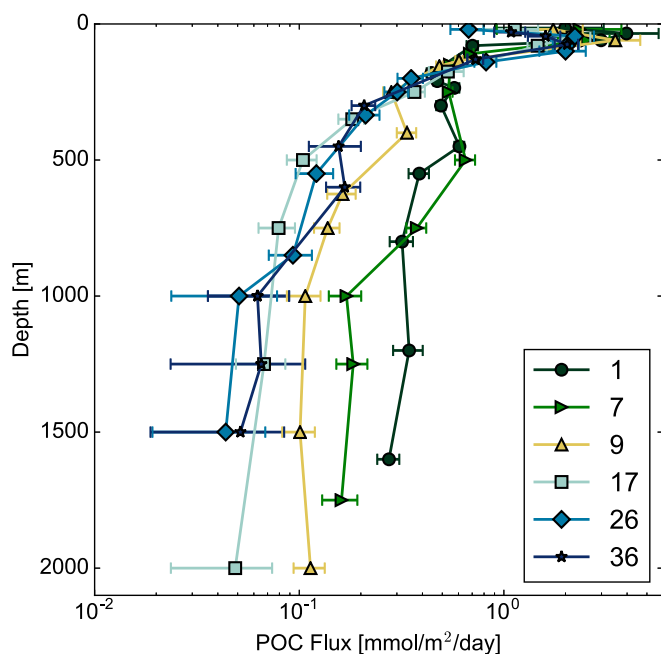


Fig. 2. $^{230}\text{Th}_p$ -normalized POC fluxes from six representative GP16 stations. The highest POC fluxes at the surface and subsurface are found at stations 1 to 9, closest to the Peru coast. Stations 17, 26, and 36, representative of the SPSG, have lower POC fluxes.

approach that included constraints from particle imaging ($b = 0.84$) (12). Our results are much more consistent with neutrally buoyant sediment trap deployments in the North Pacific subtropical gyre ($b = 1.33 \pm 0.15$), which had greater resolution through the upper water column depths at which the bulk of POC regeneration occurs (10). Transfer efficiencies derived from b values fitted to bottom-moored sediment trap observations may not be an ideal benchmark for evaluating biogeochemical model representations of POC flux and regeneration in the mesopelagic, as previously suggested (9, 20).

POC fluxes are constant with depth within the suboxic waters of the Peru ODZ (Fig. 4A). Correlations of POC flux with depth from 60 to 600 m show that the stations within the ODZ have no statistically significant decrease in POC flux with depth (Fig. 4A), while stations with no suboxic waters have highly statistically significant ($P < 10^{-10}$) decreasing POC flux in the same depth range (Fig. 4B). Stations 1 and 7 in the Peru ODZ have lower b values of 0.74 ± 0.15 and 0.66 ± 0.18 , respectively, compared with a range of b values from 1.11 to 1.52 at oxic stations 15 to 36 (Fig. 3). Previous studies have also found low b values for POC flux profiles from sediment trap deployments in ODZs, attributed to greater POC preservation under low oxygen conditions (21–23). However, the goodness of fit for power laws at stations 1 to 7, where the POC flux at depth is greatest and the top of the ODZ is shallowest, was much lower than at the offshore stations (SI Appendix, Fig. S4). The residuals of the power-law fits to stations 1 to 7 are also correlated with depth ($\rho = -0.66$, $P = 0.002$), indicating that a power law fails to adequately capture the functional form of POC flux profiles at ODZ stations.

We instead fit POC flux profiles using an exponential function (13, 24), $F_z = F_{z_0} \exp\left(-\frac{z}{L}\right) + F_\infty$, including an asymptotic flux F_∞ preserved as depth approaches infinity to quantify the effect of the ODZ on POC regeneration length scale (L) and transfer to the deep ocean. Unlike the power law, the residuals of exponential fits at ODZ stations are not significantly correlated with depth ($\rho = -0.18$, $P = 0.40$). We used the exponential fits to generate bootstrapped probability distribution functions for L and F_∞ for suboxic and oxic station groupings. The distributions are nearly disjoint, with suboxic stations having both shallower regeneration (Fig. 4C) and nearly 4 times more carbon flux preserved into the deep ocean (Fig. 4D) than oxic stations. This is not simply a consequence of larger export fluxes at suboxic stations. The transfer efficiency, computed as the best-fit F_∞/F_{\max} where F_{\max} is the maximum POC flux at each station, is 2 to 5 times higher at suboxic stations 5, 1, and 7 than at oxic stations (SI Appendix, Fig. S5). Thus, the flux profiles at suboxic stations are qualitatively and significantly different from those at oxic stations. We argue that the low b values previously inferred in ODZs overlook the importance of shallow POC regeneration in

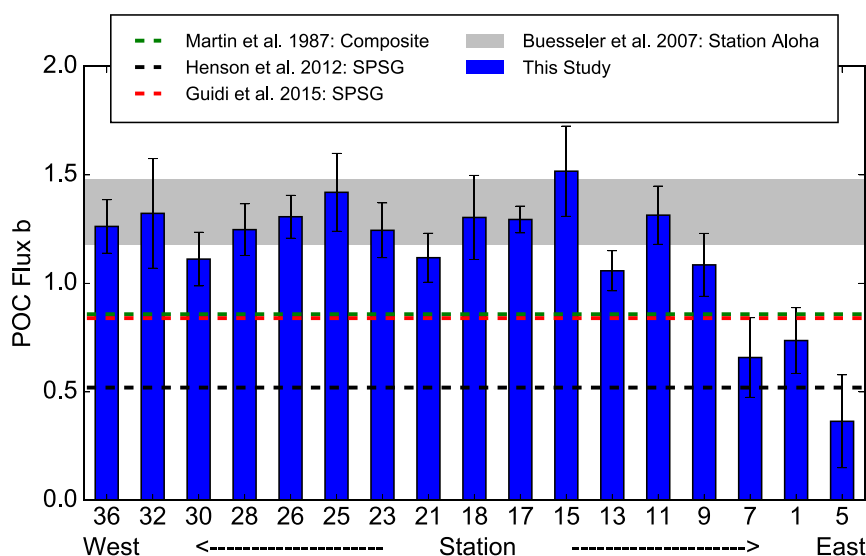


Fig. 3. Power-law b values for GP16 POC fluxes. Values from the GP16 section (blue bars, this study) are compared with a composite estimate from the North Pacific (green dashed line) (8), a neutrally buoyant sediment trap deployment from Station ALOHA in the North Pacific subtropical gyre (gray band) (10), and estimates for the SPSG derived either from combining ^{234}Th with deep-moored sediment traps (black dashed line) (11) or from particle imaging (red dashed line) (12).

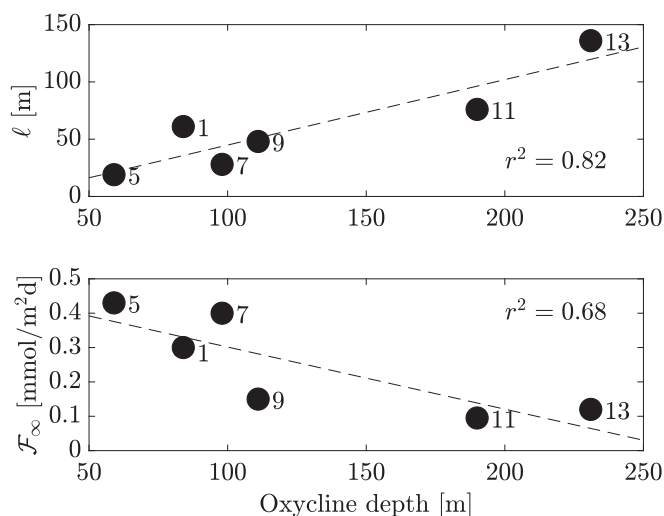


Fig. 5. Correlations of regeneration characteristics with the depth of the top of the ODZ. Both POC regeneration length scale L (*Upper*) and POC preservation to depth F_{∞} (*Lower*), derived from exponential fits to POC fluxes at each station (see *Materials and Methods*), are correlated with the depth of the upper boundary of the ODZ [defined as the depth of the appearance of curvature in uncorrected upcast SBE42 oxygen sensor data (19)], indicating that POC regeneration characteristics are strongly controlled by the presence of suboxic waters.

60-mL Savillex jars, a ^{229}Th - ^{233}Pa spike and 25 mg of purified iron carrier were added, and the filters sat overnight in concentrated HNO_3 at room temperature. The filters were then completely digested in concentrated perchloric acid (HClO_4) to dissolve the polyethersulfone material. Particles were subsequently digested in concentrated HNO_3 and HF, followed by iron coprecipitation. Thorium fractions were isolated using anion exchange chromatography (Bio-Rad AG1-X8, 100 to 200 μm). Measurements of ^{230}Th and ^{232}Th were made on a Thermo Element XR inductively coupled plasma mass spectrometer (ICP-MS) instrument, using an Aridus desolvating nebulizer for sample introduction to improve sensitivity (38). Full details of the LDEO method have been published previously (36, 39).

At UMN, one-eighth-filter aliquots were folded into 30-mL Teflon beakers, a ^{229}Th - ^{233}Pa spike was added, and filters were submerged in 7N HNO_3 and 10 drops of concentrated HF. The beakers were capped and heated under pressure for 10 h at 200 °F to leach/digest the samples. After heating, the leach solution was quantitatively transferred to a separate 30-mL Teflon beaker, and five drops of concentrated HClO_4 were added. The leach solution was dried down and taken up in 2N HCl, followed by iron hydroxide coprecipitation. The precipitate was dissolved, dried down, and taken up again in 7N HNO_3 , which was then loaded onto Bio-Rad AG1-X8 100- to 200- μm mesh resin for separation of Th fractions via anion exchange chromatography. Thorium isotope measurements were made on a Thermo Neptune multicollector ICP-MS instrument (40, 41). In both laboratories, measured ^{230}Th and ^{232}Th were blank corrected using average dipped blank values. Errors in measured ^{230}Th include uncertainties from ICP-MS counting statistics, spike concentrations, and blank corrections. Particulate ^{230}Th and ^{232}Th data are archived at BCO-DMO (<https://www.bco-dmo.org/dataset/676231>) and in the GEOTRACES Intermediate Data Product (37). More details on the measurements techniques in this study can be found in *SI Appendix, Supplementary Information Text*.

Application of ^{230}Th normalization to POC fluxes. ^{230}Th normalization is a widely used method in paleoceanography for correcting sediment mass accumulation rates for syndepositional redistribution (42, 43). Most ^{230}Th in seawater is produced in the water column by the decay of ^{234}U . Uranium is highly soluble in seawater, stabilized as carbonate complexes (44, 45) with a residence time of hundreds of thousands of years (46). As such, uranium is conservative in seawater, with only minor (parts per thousand) spatial variations in concentration as a function of salinity, allowing for the prediction of oceanic uranium concentrations from salinity (47, 48). These uranium–salinity relationships are used to predict the activity of the major uranium isotope, ^{238}U , which is multiplied by the seawater $^{234}\text{U}/^{238}\text{U}$ activity ratio of

1.1468 (49) to estimate ^{234}U . Thus, the production rate of ^{230}Th integrated to a depth horizon z can be predicted anywhere in the water column:

$$P(^{230}\text{Th})_z = \int_0^z \lambda_{230} {}^{234}\text{U} \, dz.$$

Unlike its parent ^{234}U , ^{230}Th is highly insoluble in seawater. Upon production by ^{234}U decay, ^{230}Th rapidly adsorbs to particles, with a scavenging residence time of 20 to 40 y (50), much shorter than both its half-life [75,584 y (51)] and the time scale of whole-ocean mixing. The removal of ^{230}Th from a given location is potentially driven by two processes: scavenging removal by particles, and lateral redistribution by advective-diffusive fluxes. Where the latter can be either ignored or corrected, the concentrations of both dissolved and particulate ^{230}Th are expected to increase linearly with depth in a process known as reversible scavenging (52). In this formulation, the integrated production of ^{230}Th to a depth z is balanced in one dimension by its downward export on particles sinking through that depth.

The equation for calculating $^{230}\text{Th}_p$ -normalized POC fluxes is nearly identical to that used in paleoceanography to determine vertical constituent fluxes:

$$POCFlux = \frac{P(^{230}Th)_z * [POC]}{[^{230}Th]_0},$$

where the integrated production rate is in $\mu\text{Bq}\cdot\text{m}^{-2}\cdot\text{d}^{-1}$, $[^{230}\text{Th}]_p$ is the activity of particulate ^{230}Th in $\mu\text{Bq}\cdot\text{m}^{-3}$, and $[\text{POC}]$ is the concentration of POC in $\text{mmol}\cdot\text{m}^{-3}$. The resulting POC fluxes we report ([Dataset S1](#)) are in units of $\text{mmol}\cdot\text{m}^{-2}\cdot\text{d}^{-1}$.

We calculate POC fluxes on particles in the 0.8- to 51- μm SSF. Due to low ^{230}Th activity on particles $>51\text{ }\mu\text{m}$, larger filter aliquots were required for analysis than could be routinely measured across the entire section. The actual size of sinking particles carrying ^{230}Th downward to balance its water column production is unknown. However, scavenging removal of ^{230}Th is a two-step process involving adsorption of ^{230}Th onto small particles, which subsequently undergo repeated cycles of aggregation into larger "sinking" particles and disaggregation into smaller "suspended" particles (53, 54). Thus, provided that the aggregation-sinking process is in equilibrium on the time scales of ^{230}Th removal, the POC fluxes recorded by $^{230}\text{Th}_p$ normalization on 0.8- to 51- μm particles will be valid.

Statistical procedures. Power laws of form $F_z = F_{z_0} \left(\frac{z}{z_0} \right)^{-\alpha}$ were fit to POC flux profiles at each station (Fig. 3) using data only at or above 1,000 m. Because the depths of the mixed layer, the deep chlorophyll maximum, and the oxycline varied between stations (*SI Appendix, Fig. S2*), we used the depth of maximum POC flux at each station as the reference depth z_0 rather than interpolating onto a common reference depth (e.g., the base of the euphotic zone or 100 m) across all stations. We show in *SI Appendix, Supplementary Information Text* that our findings are not sensitive to the choice of reference depth.

For Fig. 4 A and B, data from the suboxic stations at the depths where oxygen concentrations were near zero (60 to 600 m) were grouped, as were data from the oxic stations over the same depth range. Three correlation tests were performed—Pearson's correlation, Spearman's rank correlation, and Kendall's rank correlation (also known as Kendall's tau)—and associated *P* values were computed for both groups of data (55). By any usual significance threshold, fluxes from suboxic depths of the suboxic stations are not significantly correlated with depth, whereas fluxes from the same depths of the oxic stations significantly decrease with depth.

To quantify the differences between the flux–depth relationships in the oxic versus suboxic stations, we estimated uncertainty in the parameters of the exponential fits using a bootstrap analysis (56). For each group of stations, we generated 10,000 replicate datasets via resampling with replacement and then fit the functional form $F_z = F_{z_0} \exp\left(-\frac{z}{L}\right) + F_{\infty}$ via nonlinear least-squares regression to each replicate. These 10,000 estimates for each parameter are shown in Fig. 4 C and D for F_{∞} and L , respectively. Based on the intersection of these parameters' estimated probability distributions, we can state with 98% and 90% confidence, respectively, that F_{∞} is larger and that L is smaller for the suboxic data than for the oxic data. The median L for the suboxic data is 56 m and the median L for the oxic data is 102 m. The median F_{∞} for the suboxic data is 0.36 mmol·m⁻²·d⁻¹ and the median F_{∞} for the oxic data is 0.093 mmol·m⁻²·d⁻¹.

ACKNOWLEDGMENTS. We thank the captain and crew of the Research Vessel *Thomas G. Thompson* during the TN303 cruise. The pump team led by Dan Ohnemus was responsible for the collection of the particulate samples

used in this study. We thank Cassandra Costa for comments on an early draft of the paper, as well as two anonymous reviewers and the handling editor for constructive feedback. This work was funded by US National Science

Foundation Awards OCE-1233688 (to R.F.A.), OCE-1233903 (to R.L.E.), and OCE-1518110 (to P.J.L.), and by the NSF Graduate Research Fellowship DGE-16-44869 (to F.J.P.).

- Hain MP, Sigman DM, Haug GH (2013) The biological pump in the past. *Treatise on Geochemistry*, eds Holland HD, Turekian KK (Elsevier, Oxford), 2nd Ed, Vol. 8, pp 485–517.
- De La Rocha CL, Passow U (2014) The biological pump. *Treatise on Geochemistry*, eds Holland HD, Turekian KK (Elsevier, Oxford), 2nd Ed, Vol 8, pp 93–122.
- Behrenfeld MJ, Falkowski PG (1997) Photosynthetic rates derived from satellite-based chlorophyll concentration. *Limnol Oceanogr* 42:1–20.
- Behrenfeld MJ, et al. (2001) Biospheric primary production during an ENSO transition. *Science* 291:2594–2597.
- Siegel DA, et al. (2014) Global assessment of ocean carbon export by combining satellite observations and food-web models. *Global Biogeochem Cycles* 28:181–196.
- Henson SA, et al. (2011) A reduced estimate of the strength of the ocean's biological carbon pump. *Geophys Res Lett* 38:L04606.
- Kwon EY, Primeau F, Sarmiento JL (2009) The impact of remineralization depth on the air–sea carbon balance. *Nat Geosci* 2:630–635.
- Martin JH, Knauer GA, Karl DM, Broenkow WW (1987) VERTEX: Carbon cycling in the northeast Pacific. *Deep Sea Res A Oceanogr Res Pap* 34:267–285.
- Marsay CM, et al. (2015) Attenuation of sinking particulate organic carbon flux through the mesopelagic ocean. *Proc Natl Acad Sci USA* 112:1089–1094.
- Buesseler KO, et al. (2007) Revisiting carbon flux through the ocean's twilight zone. *Science* 316:567–570.
- Henson SA, Sanders R, Madsen E (2012) Global patterns in efficiency of particulate organic carbon export and transfer to the deep ocean. *Global Biogeochem Cycles* 26:GB1028.
- Guidi L, et al. (2015) A new look at ocean carbon remineralization for estimating deepwater sequestration. *Global Biogeochem Cycles* 29:1044–1059.
- Armstrong RA, Lee C, Hedges JL, Honjo S, Wakeham SG (2002) A new, mechanistic model for organic carbon fluxes in the ocean based on the quantitative association of POC with ballast minerals. *Deep Sea Res Part II Top Stud Oceanogr* 49:219–236.
- Francois R, Frank M, Rutgers van der Loeff MM, Bacon MP (2004) ^{230}Th normalization: An essential tool for interpreting sedimentary fluxes during the late Quaternary. *Paleoceanography* 19:PA1018.
- Hirose K (2006) A new method to determine depth-dependent carbon export fluxes using vertical ^{230}Th profiles. *Geophys Res Lett* 33:L05609.
- Anderson RF, et al. (2016) How well can we quantify dust deposition to the ocean? *Philos Trans A Math Phys Eng Sci* 374:20150285.
- Hayes CT, et al. (2018) Flux of particulate elements in the North Atlantic Ocean constrained by multiple radionuclides. *Global Biogeochem Cycles* 32:1738–1758.
- Thamdrup B, Dalsgaard T, Revsbech NP (2012) Widespread functional anoxia in the oxygen minimum zone of the Eastern South Pacific. *Deep Sea Res Part I Oceanogr Res Pap* 65:36–45.
- Ohnemus DC, et al. (2017) Elevated trace metal content of prokaryotic communities associated with marine oxygen deficient zones. *Limnol Oceanogr* 62:3–25.
- Weber T, Cram JA, Leung SW, DeVries T, Deutsch C (2016) Deep ocean nutrients imply large latitudinal variation in particle transfer efficiency. *Proc Natl Acad Sci USA* 113:8606–8611.
- Van Mooy BAS, Keil RG, Devol AH (2002) Impact of suboxia on sinking particulate organic carbon: Enhanced carbon flux and preferential degradation of amino acids via denitrification. *Geochim Cosmochim Acta* 66:457–465.
- Cavan EL, Trimmer M, Shelley F, Sanders R (2017) Remineralization of particulate organic carbon in an ocean oxygen minimum zone. *Nat Commun* 8:14847.
- Keil RG, Neibauer JA, Biladeau C, van der Elst K, Devol AH (2016) A multiproxy approach to understanding the “enhanced” flux of organic matter through the oxygen-deficient waters of the Arabian Sea. *Biogeosciences* 13:2077–2092.
- Buesseler KO, Boyd PW (2009) Shedding light on processes that control particle export and flux attenuation in the twilight zone of the open ocean. *Limnol Oceanogr* 54:1210–1232.
- Babbin AR, Keil RG, Devol AH, Ward BB (2014) Organic matter stoichiometry, flux, and oxygen control nitrogen loss in the ocean. *Science* 344:406–408.
- Sarmiento JL, et al. (2004) Response of ocean ecosystems to climate warming. *Global Biogeochem Cycles* 18:GB3003.
- Polovina JJ, Howell EA, Abecassis M (2008) Ocean's least productive waters are expanding. *Geophys Res Lett* 35:270.
- Stramma L, Johnson GC, Sprintall J, Mohrholz V (2008) Expanding oxygen-minimum zones in the tropical oceans. *Science* 320:655–658.
- Gilly WF, Beman JM, Litvin SY, Robison BH (2013) Oceanographic and biological effects of shoaling of the oxygen minimum zone. *Annu Rev Mar Sci* 5:393–420.
- Oschlies A, Brandt P, Stramma L, Schmidt S (2018) Drivers and mechanisms of ocean deoxygenation. *Nat Geosci* 11:467–473.
- Breitbart D, et al. (2018) Declining oxygen in the global ocean and coastal waters. *Science* 359:eaam7240.
- Bishop JKB, Lam PJ, Wood TJ (2012) Getting good particles: Accurate sampling of particles by large volume in-situ filtration. *Prog Oceanogr* 10:681–710.
- Lam PJ, et al. (2018) Size-fractionated distributions of suspended particle concentration and major phase composition from the U.S. GEOTRACES Eastern Pacific Zonal Transect (GP16). *Mar Chem* 201:90–107.
- Lee JM, Heller MI, Lam PJ (2018) Size distribution of particulate trace elements in the U.S. GEOTRACES Eastern Pacific Zonal Transect (GP16). *Mar Chem* 201:108–123.
- Peters BD, et al. (2018) Water mass analysis of the 2013 US GEOTRACES eastern Pacific zonal transect (GP16). *Mar Chem* 201:6–19.
- Pavia F, et al. (2018) Intense hydrothermal scavenging of ^{230}Th and ^{231}Pa in the deep Southeast Pacific. *Mar Chem* 201:212–228.
- Schlitzer R, et al. (2018) The GEOTRACES Intermediate Data Product 2017. *Chem Geol* 493:210–223.
- Choi MS, et al. (2001) Rapid determination of ^{230}Th and ^{231}Pa in seawater by desolvated micro-nebulization inductively coupled plasma magnetic sector mass spectrometry. *Mar Chem* 76:99–112.
- Anderson RF, et al. (2012) GEOTRACES intercalibration of ^{230}Th , ^{232}Th , ^{231}Pa , and prospects for ^{10}Be . *Limnol Oceanogr Methods* 10:179–213.
- Shen C-C, et al. (2012) High-precision and high-resolution carbonate ^{230}Th dating by MC-ICP-MS with SEM protocols. *Geochim Cosmochim Acta* 99:71–86.
- Shen C-C, et al. (2002) Uranium and thorium isotopic and concentration measurements by magnetic sector inductively coupled plasma mass spectrometry. *Chem Geol* 185:165–178.
- Henderson GM, Anderson RF (2003) The U-series toolbox for paleoceanography. *Rev Mineral Geochem* 52:493–531.
- Bacon MP (1984) Glacial to interglacial changes in carbonate and clay sedimentation in the Atlantic Ocean estimated from ^{230}Th measurements. *Chem Geol* 46:97–111.
- Djogić R, Sipos L, Branica M (1986) Characterization of uranium(VI) in seawater. *Limnol Oceanogr* 31:1122–1131.
- Langmuir D (1978) Uranium solution-mineral equilibria at low temperatures with applications to sedimentary ore deposits. *Geochim Cosmochim Acta* 42:547–569.
- Dunk RM, Mills RA, Jenkins WJ (2002) A reevaluation of the oceanic uranium budget for the Holocene. *Chem Geol* 190:45–67.
- Chen JH, Edwards RL, Wasserburg GJ (1986) ^{238}U , ^{234}U and ^{232}Th in seawater. *Earth Planet Sci Lett* 80:241–251.
- Owens SA, Buesseler KO, Sims KWW (2011) Re-evaluating the ^{238}U -salinity relationship in seawater: Implications for the ^{238}U - ^{234}Th disequilibrium method. *Mar Chem* 127:31–39.
- Andersen MB, Stirling CH, Zimmermann B, Halliday AN (2010) Precise determination of the open ocean $^{234}\text{U}/^{238}\text{U}$ composition. *Geochem Geophys Geosyst* 11:Q12003.
- Hayes CT, et al. (2013) A new perspective on boundary scavenging in the North Pacific Ocean. *Earth Planet Sci Lett* 369–370:86–97.
- Cheng H, et al. (2013) Improvements in ^{230}Th dating, ^{230}Th and ^{234}U half-life values, and U–Th isotopic measurements by multi-collector inductively coupled plasma mass spectrometry. *Earth Planet Sci Lett* 371–372:82–91.
- Bacon MP, Anderson RF (1982) Distribution of thorium isotopes between dissolved and particulate forms in the deep sea. *J Geophys Res* 87:2045–2056.
- Bacon MP, Huh C-A, Fleer AP, Deuser WG (1985) Seasonality in the flux of natural radionuclides and plutonium in the deep Sargasso Sea. *Deep Sea Res A Oceanogr Res Pap* 32:273–286.
- Wang W-L, Armstrong RA, Cochran JK, Heilbrun C (2016) ^{230}Th and ^{234}Th as coupled tracers of particle cycling in the ocean: A maximum likelihood approach. *Deep Sea Res Part I Oceanogr Res Pap* 111:61–70.
- Press WH, Teukolsky SA, Vetterling WT, Flannery BP (1992) *Numerical Recipes in C: The Art of Scientific Computing* (Cambridge Univ Press, Cambridge, UK), 2nd Ed.
- Efron B (1979) Bootstrap methods: Another look at the jackknife. *Ann Stat* 7:1–26.



Supplementary Information for

Shallow Particulate Organic Carbon Regeneration in the South Pacific Ocean

Frank J. Pavia, Robert F. Anderson, Phoebe J. Lam, B.B. Cael, Sebastian M. Vivancos, Martin Q. Fleisher, Yanbin Lu, Pu Zhang, Hai Cheng, R. Lawrence Edwards

Frank J. Pavia

Email: fpavia@ldeo.columbia.edu

This PDF file includes:

Supplementary text

Figs. S1 to S7

References for SI reference citations

Supplementary Information Text

Determining Unsupported $^{230}\text{Th}_{\text{xs}}$ for computing POC fluxes. Calculating ^{230}Th -normalized fluxes requires that the ^{230}Th is only sourced from the decay of ^{234}U in the water column. However, there is lithogenic particulate ^{230}Th from two separate sources: ^{230}Th supported by ^{234}U in the mineral lattice of detrital particles brought to the ocean by dust or resuspended sediments, and ^{230}Th released during sediment dissolution that subsequently adsorbs onto particles (1). This correction is performed by subtracting the product of measured particulate ^{232}Th and the lithogenic $^{230}\text{Th}/^{232}\text{Th}$ ratio (4×10^{-6} mole/mole) (2) from measured $^{230}\text{Th}_{\text{p}}$. All $^{230}\text{Th}_{\text{p}}$ data reported in this paper and used in flux calculations are corrected in this manner. Additional uncertainties from the measured $^{232}\text{Th}_{\text{p}}$ and a nominal 30% uncertainty in the lithogenic $^{230}\text{Th}/^{232}\text{Th}$ ratio are propagated into the reported error in $^{230}\text{Th}_{\text{p}}$.

Total ^{230}Th is computed as the sum of small particulate and dissolved ^{230}Th . Where possible, dissolved samples were taken at identical depths as particulate samples, but otherwise were interpolated onto the depths of $^{230}\text{Th}_{\text{p}}$ for calculating total ^{230}Th . Full details of the methods for collecting and measuring dissolved ^{230}Th on the GP16 section have been previously reported (3). Samples were taken from a conventional stainless-steel rosette in Niskin bottles, and 4-5 liters of water were filtered through a $0.45\mu\text{m}$ Acropak capsule filter. The samples were acidified to $\text{pH}=2$ at sea using 6M ultrapure HCl to prevent adsorption of Th to cubitainer walls during transport to shore (4). In the lab, samples were weighed and spiked with ^{229}Th - ^{233}Pa , co-precipitated with iron oxyhydroxide, and digested in HNO_3 , HF, and HClO_4 . Separation of Th fractions by anion exchange chromatography and measurement by ICP-MS followed the same

methodology described for particulate samples. Measured dissolved ^{230}Th was corrected for ingrowth by ^{234}U during sample storage.

Testing Possible Biases in ^{230}Th -derived POC fluxes. We test the validity of using the 0.8-51 μm particle size class by comparing $^{230}\text{Th}_\text{p}$ -normalized 0.8-51 μm POC fluxes with results from annually-averaged bottom-moored sediment traps. Hayes et al. (16) found that $^{230}\text{Th}_\text{p}$ -derived POC fluxes below 1000m were within 8% and 21% of multi-year averages from collocated deep moored sediment traps at the Bermuda Atlantic Time-Series. On the GP16 section, $^{230}\text{Th}_\text{p}$ -derived POC fluxes agree closely with annual POC fluxes from nearby deep sediment traps (7, 8). At 135°W, sediment trap POC fluxes are within 1-sigma uncertainty of $^{230}\text{Th}_\text{p}$ -derived fluxes at similar depths (*SI Appendix* Fig. S1a), while at 100°W, $^{230}\text{Th}_\text{p}$ -normalized fluxes at 14°S and 16°S are halfway between the sediment trap values at 10°S and 20°S, capturing the regional latitudinal productivity gradient (*SI Appendix*, Fig. S1b). The close agreement between the $^{230}\text{Th}_\text{p}$ -normalized fluxes of 0.8-51 μm POC and sediment trap estimates indicates that aggregation-disaggregation between small and large particles is of primary importance for the downward transfer of POC in the mesopelagic and bathypelagic, in agreement with optical particle observations (9) and biomarker ^{13}C results (10).

We test whether size fractionation is a potential bias by comparing >51 μm and 0.8-51 μm POC/ $^{230}\text{Th}_\text{p}$ ratios for the limited number of samples for which it was possible to analyze both size fractions (*SI Appendix* Fig. S6). POC/ $^{230}\text{Th}_\text{p}$ is $29 \pm 6\%$ higher in the >51 μm size fraction ($n=23$, $R^2=0.95$), but there is no appreciable trend in size fractionation with depth. Not including a single high POC/ $^{230}\text{Th}_\text{p}$ value in both size

fractions from station 7 that drives the most of the correlation, the best-fit $\text{POC}/^{230}\text{Th}_p$ slope is 1.05 ± 0.11 ($n=22$, $R^2=0.8$), within uncertainty of unity (*SI Appendix*, Fig. S6). So, while it is possible that our fluxes derived from $0.8\text{-}51\mu\text{m}$ particles slightly underestimate the overall POC flux, this should not affect our interpretation of the shape of the profiles (i.e., the gradient with depth in the POC flux).

The POC fluxes we observe are also not influenced by lateral transport of organic matter from the continental shelf. Sanial et al. (11) measured ^{228}Ra , which is supplied by diffusion from sediments and thus traces the advection of material from the continental shelf, on the GP16 section. While ^{228}Ra is enriched in the surface stations from the shelf to the open ocean, the enrichment is mostly confined to oxic waters above the OMZ, indicating low lateral inputs of shelf-derived material to ODZ depths (11). Additionally, the offshore gradient in POC flux within the ODZ is minimal (Fig. 1, *SI Appendix* Fig. S3), whereas lateral transport of POC from the shelf would likely cause there to be much higher POC fluxes near the shelf that drop off rapidly towards the open ocean.

Application of $^{230}\text{Th}_p$ -normalization requires there to be no net advective and/or diffusive gain or loss of ^{230}Th in the water column. Lateral transport of ^{230}Th could potentially bias ^{230}Th -normalized fluxes. High particle fluxes in productive regions could result in lower dissolved ^{230}Th concentrations than in oligotrophic regions with low particles fluxes. Lateral eddy diffusion could then transport ^{230}Th from the interior towards the margin, a process known as boundary scavenging (12, 13). The short residence time of ^{230}Th generally limits its redistribution by lateral isopycnal diffusion (14), and annually-averaged sediment trap fluxes of ^{230}Th are typically within 10-15% of the production rate in the overlying water column (15). A slight zonal gradient in

dissolved and total ^{230}Th is apparent in our profiles below 400m (*SI Appendix*, Fig. S7). Net shoreward transport of ^{230}Th by mixing would act to increase the apparent $^{230}\text{Th}_p$ -normalized POC fluxes at sites further offshore, and decrease them close to shore. However, there is no discernable feature in the POC flux profiles below 400m that would indicate shoreward transport of ^{230}Th at these depths, and the bulk of the differences between POC flux profiles is above the depths where there is an offshore ^{230}Th gradient. Additionally, both surface (16) and 400m subsurface (17) net zonal flows at 8-12°S are negligible. Thus, lateral transport by either advection or eddy diffusion does not impact our results.

Upwelling rates of 0-3 m d⁻¹ have been estimated in nearshore waters off Peru using ^3He and ^7Be methods (18-20). Since total ^{230}Th increases with depth, upwelling can transport ^{230}Th upward through the base of the mixed layer. In this case, the sinking flux of particulate ^{230}Th will be balanced by its production from ^{234}U decay and its supply from upwelling. Adding an upwelling flux would increase the $^{230}\text{Th}_p$ -derived POC flux estimates in the uppermost water column, making our maximum flux estimates a lower bound. However, we focus our interpretations on the depth-dependence of POC regeneration rates, which is not influenced by upwelling. If the shape of the regeneration profile were dictated by the upwelling of ^{230}Th , we would expect this to be a consistent feature across stations influenced by upwelling, whereas the regeneration features instead track the depth of the oxycline (Fig. 5). Further, performing statistical analysis of the POC regeneration length scales only by station groupings averages out any potential effects of upwelling at a single station.

Testing Possible Biases in Choice of Reference Depth. The choice of reference depth can affect the b values for power law fits of POC flux profiles (21). We compare b and reference depth z_0 from the GP16 section (*SI Appendix*, Fig. S8), finding a weak positive correlation between b and z_0 ($R^2=0.27$, $p=0.034$, $n=17$). This correlation is in the opposite direction of what we would expect to find if shallow reference depths were driving artificially high b values. We also show that the location of reference depth relative to the MLD and DCM does not bias our b estimates. At some stations, the reference depth z_0 falls slightly above the DCM (15,21,23,25,28) or above both the DCM and MLD (5,11,13,17,26). In these cases, the POC/ ^{230}Th ratio could potentially be offset from the POC/ ^{230}Th ratio of sinking particles due to the contribution of POC from newly produced, non-sinking particles that are recycled *in-situ*. We test whether the inclusion of these stations biases our fitting procedures. The mean of b values from stations where z_0 is above the DCM and/or MLD (5,11,13,17,21,23,25,26,28) is 1.18 ± 0.34 , within uncertainty and very close to the mean b value of 1.09 ± 0.26 from stations where z_0 is below the MLD and DCM (1,7,9,30,32,36). Limiting the comparison only to offshore stations (11-36), the stations with z_0 above the DCM only (15,21,23,25,28) have a mean b value of 1.3 ± 0.16 , within error of and similar to the mean b values of 1.24 ± 0.12 from stations with z_0 above both the MLD and DCM (11,13,17,26), and of 1.23 ± 0.11 from stations where z_0 is deeper than both the DCM and MLD (30,32,36). We also re-fit the exponential functions at stations 11 and 13 using z_0 as the first sampling depth below the MLD and DCM to test whether the correlation in Fig. 5 is an artifact of the choice of reference depth. In this sensitivity test, the correlation between oxycline depth and L still holds, with $R^2=0.72$, as does the correlation between oxycline depth and F_∞ , with

$R^2=0.69$. We thus conclude that neither our b values, nor the correlation between oxycline depth and regeneration characteristics from exponential fitting, are artifacts of the choice of reference depth.

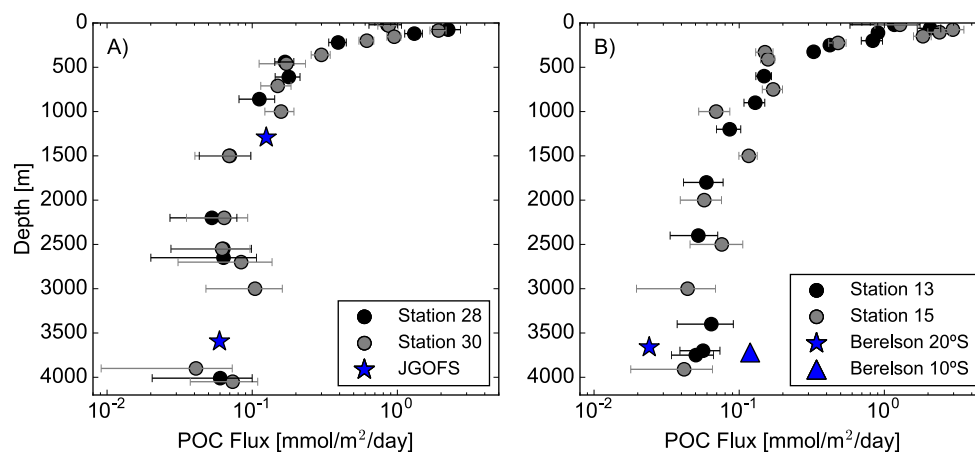


Fig. S1. Comparison between GP16 $^{230}\text{Th}_p$ -normalized POC fluxes and sediment trap estimates.

$^{230}\text{Th}_p$ -normalized fluxes from stations zonally-bracketing the sediment trap longitudes are shown as black and gray dots. Annually-averaged sediment trap fluxes are shown as blue stars or blue triangles. a, Comparison between GP16 stations 28 and 30 with sediment trap fluxes from the JGOFS program (12°S, 135°W), deployed in 1992 (7). b, Comparison between GP16 stations 13 and 15 at 14°S and 16°S with sediment trap deployments from 2010-2011 at 10°S and 20°S along 100°W (8).

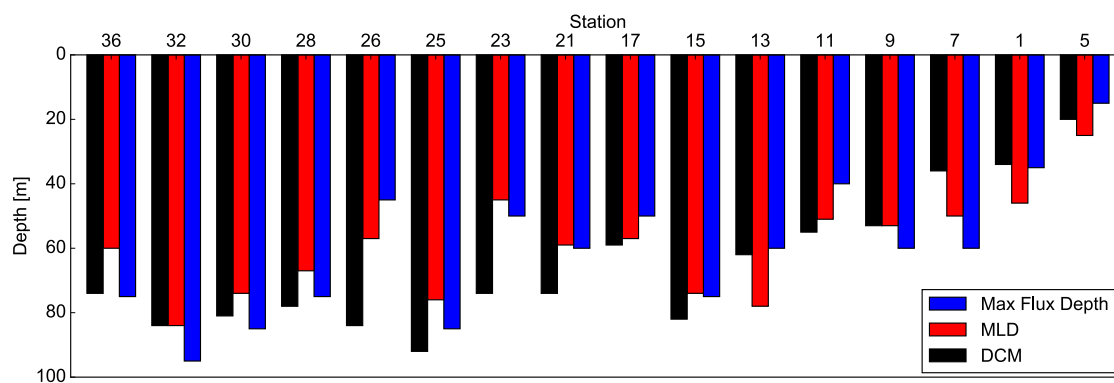


Fig. S2. Depth of Maximum POC Flux (this study), Mixed Layer Depth (MLD) **(22)** and Deep Chlorophyll Maximum (DCM) **(22)**. Station 18 is omitted because there were no $^{230}\text{Th}_p$ measurements on samples above 150m. Stations are oriented from east (right) to west (left).

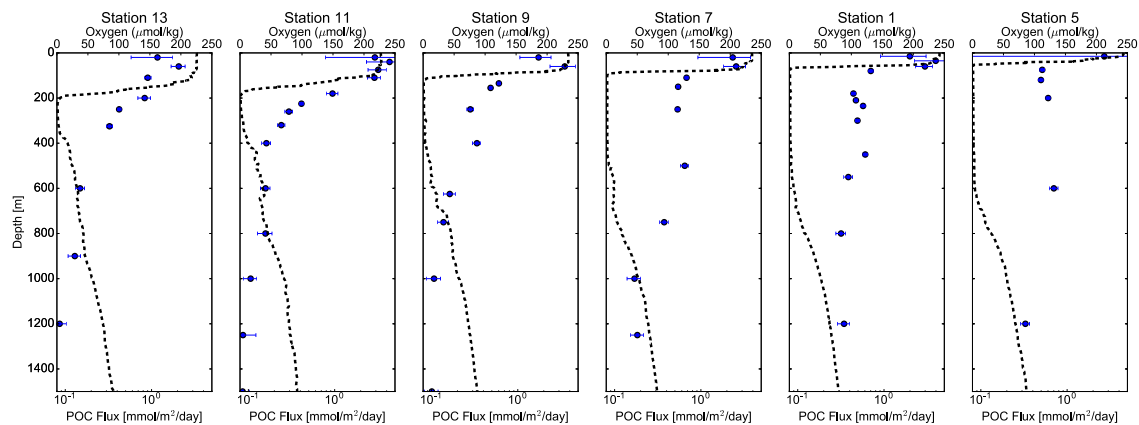


Fig. S3. POC Fluxes (blue symbols) and Oxygen Profiles (dashed lines) at GP16 Stations 1-13.

Station order is shown from east to west going right to left. The length scale of POC flux

attenuation tracks the depth of the upper oxycline at these stations.

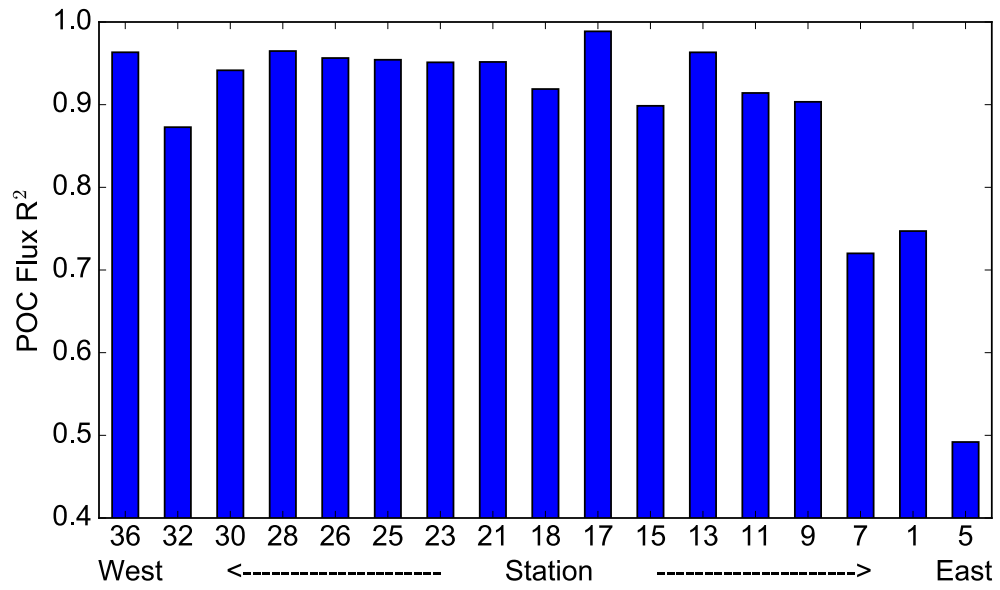


Fig. S4. R^2 values for power law fits to POC flux data. Fits are poorer at stations 5, 1, and 7, where the upper oxycline is shallowest, indicating the power laws do not properly represent the functional form of POC flux profiles at ODZ stations.

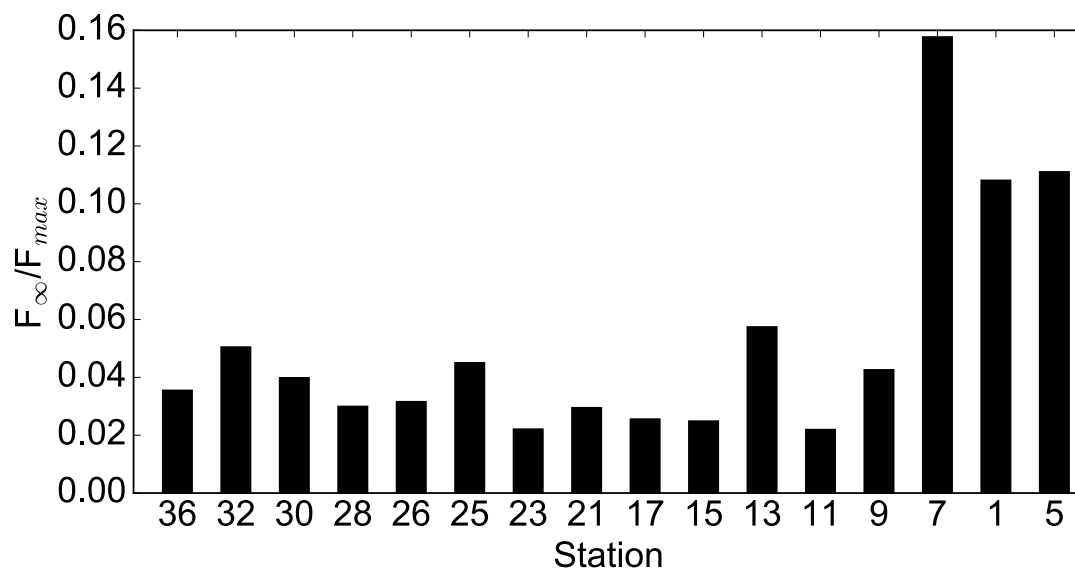


Fig. S5. Transfer efficiencies for POC fluxes. Values are computed as the ratio between the best-fit F_{∞} from exponential fits to POC flux profiles and the observed maximum POC flux at each station. Highest values at suboxic stations 5, 1, and 7 indicate greater POC preservation at the stations with thickest ODZs.

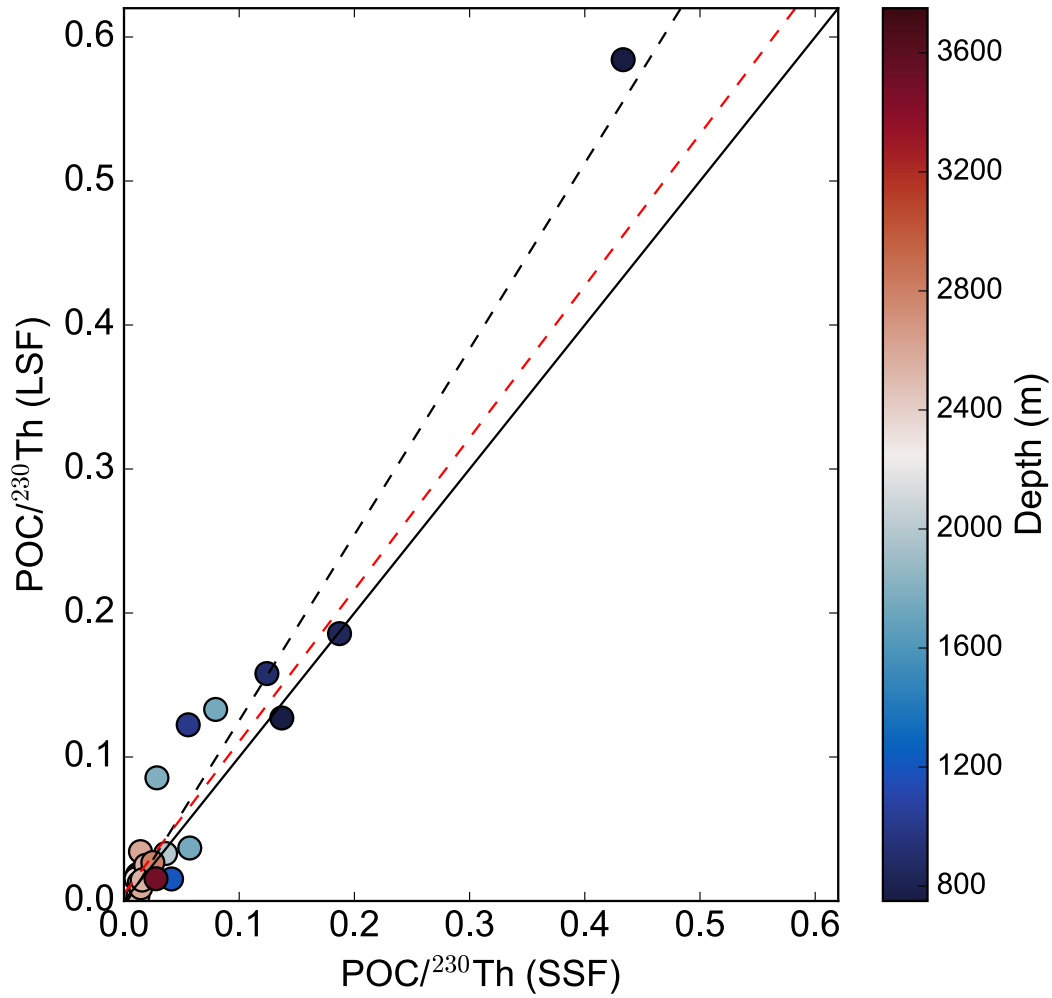


Fig. S6. Size Partitioning of $\text{POC}/^{230}\text{Th}$. Dots show individual data points of $\text{POC}/^{230}\text{Th}$ ratios in large size fraction particles (LSF, $>51\mu\text{m}$) and small size fraction particles (SSF, $0.8\text{-}51\mu\text{m}$), colored by depth. Dashed line black shows the best-fit line (slope=1.29, $n=23$, $R^2=0.95$) for all data points. Since much of the correlation is driven by a single high $\text{POC}/^{230}\text{Th}$ ratio point from 750m at Station 7, we also fit the data without this point – the best fit line excluding this point is shown as a dashed red line (slope=1.05, $n=22$, $R^2=0.81$). The 1:1 line is shown as a solid black line.

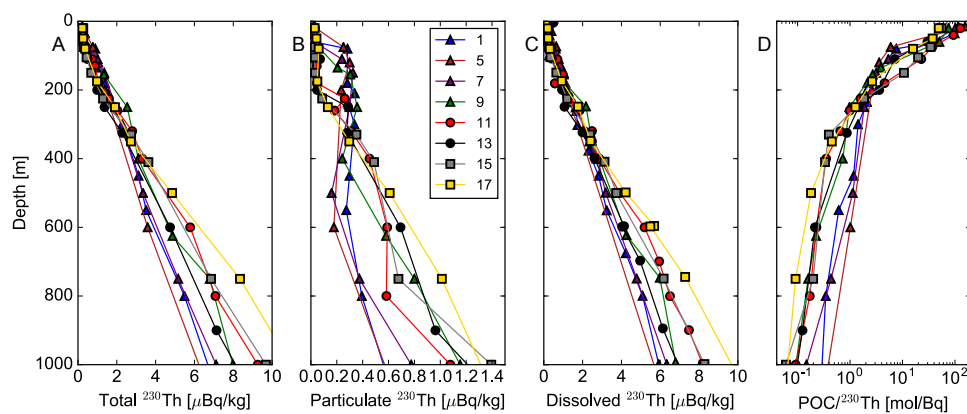


Fig. S7. ^{230}Th Profiles and POC/ ^{230}Th ratios. a, Total ^{230}Th . b, Particulate ^{230}Th . c, Dissolved ^{230}Th . d, POC/ $^{230}\text{Th}_p$ ratios. Data from ODZ stations are shown as triangles.

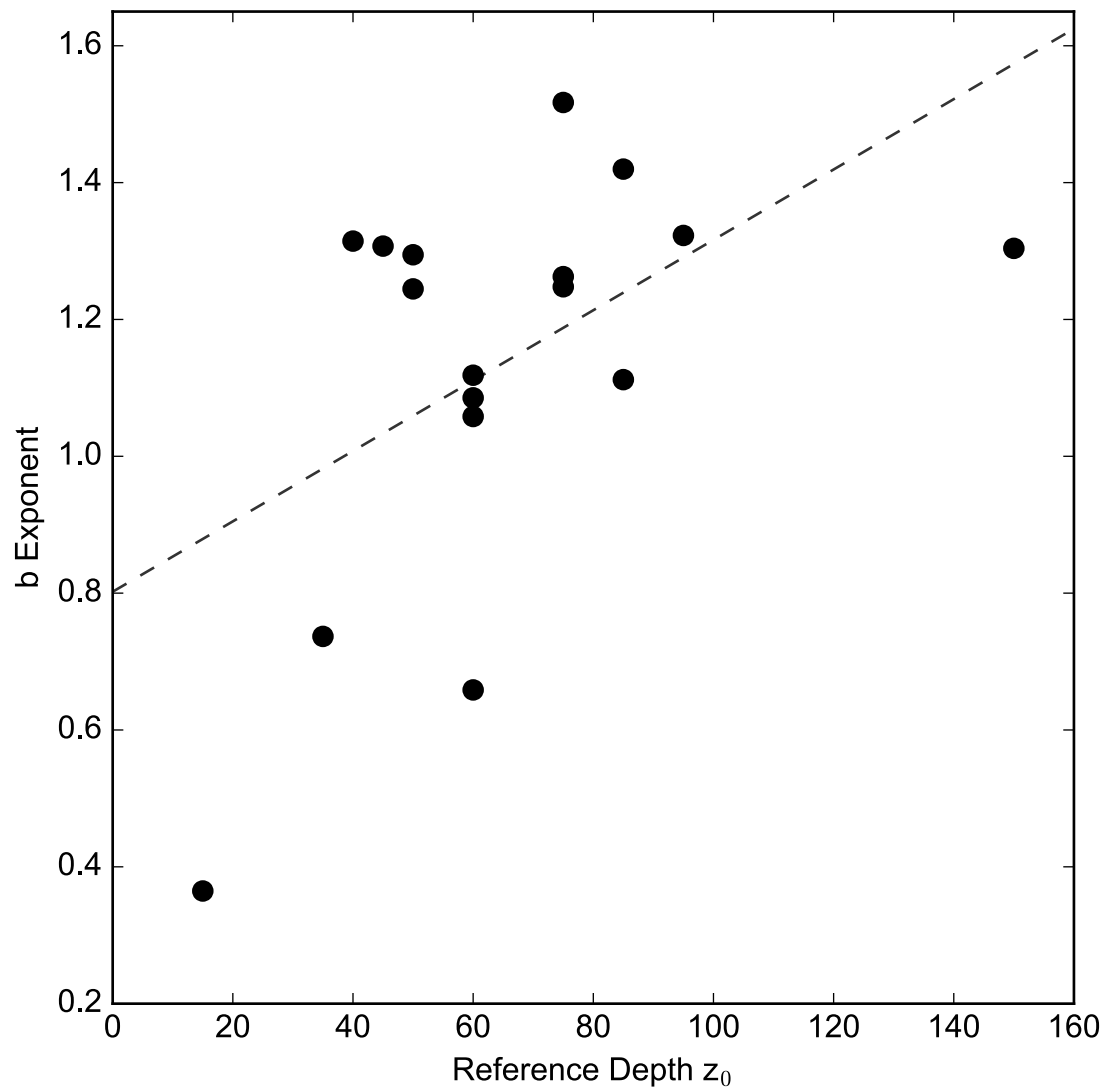


Fig. S8. Relationship of b values and reference depth z_0 . Dots show points from individual stations. Dashed line shows the least-squares linear fit to the data, which are weakly correlated with slope 0.005 ± 0.002 ($R^2=0.27$, $p=0.034$, $n=17$).

References

1. Hayes CT, et al. (2015) Intensity of Th and Pa scavenging partitioned by particle chemistry in the North Atlantic Ocean. *Marine Chemistry* 170:49–60.
2. Roy-Barman M, et al. (2009) The influence of particle composition on Thorium scavenging in the Mediterranean Sea. *Earth and Planetary Science Letters* 286(3-4):526–534.
3. Pavia F, et al. (2018) Intense hydrothermal scavenging of ^{230}Th and ^{231}Pa in the deep Southeast Pacific. *Marine Chemistry* 201:212–228.
4. Anderson RF, et al. (2012) GEOTRACES intercalibration of ^{230}Th , ^{232}Th , ^{231}Pa , and prospects for ^{10}Be . *Progress in Oceanography* 10(4):179–213.
5. Bacon MP, Huh C-A, Fleer AP, Deuser WG (1985) Seasonality in the flux of natural radionuclides and plutonium in the deep Sargasso Sea. *Deep Sea Research Part A Oceanographic Research Papers* 32(3):273–286.
6. Wang W-L, Armstrong RA, Cochran JK, Heilbrun C (2016) ^{230}Th and ^{234}Th as coupled tracers of particle cycling in the ocean: A maximum likelihood approach. *Deep Sea Research Part I: Oceanographic Research Papers* 111:61–70.
7. Hernes PJ, et al. (2001) Particulate carbon and nitrogen fluxes and compositions in the central equatorial Pacific. *Deep Sea Research Part I: Oceanographic Research Papers* 48(9):1999–2023.
8. Berelson WM, et al. (2015) Biogenic particle flux and benthic remineralization in the Eastern Tropical South Pacific. *Deep Sea Research Part I: Oceanographic Research Papers* 99:23–34.
9. Kiko R, et al. (2017) Biological and physical influences on marine snowfall at the equator. *Nature Geosci* 10(11):852–858.
10. Close HG, et al. (2013) Export of submicron particulate organic matter to mesopelagic depth in an oligotrophic gyre. *PNAS* 110(31):12565–12570.
11. Sanial V, et al. (2018) Radium-228 as a tracer of dissolved trace element inputs from the Peruvian continental margin. *Marine Chemistry* 201:20–34.
12. Bacon MP, Spencer DW, Brewer PG (1976) $^{210}\text{Pb}/^{226}\text{Ra}$ and $^{210}\text{Po}/^{210}\text{Pb}$ disequilibria in seawater and suspended particulate matter. *Earth and Planetary Science Letters* 32(2):277–296.
13. Spencer DW, Bacon MP, Brewer PG (1981) Models of the distribution of ^{210}Pb in a section across the North Equatorial Atlantic Ocean. *J Mar Res* 39(1):119–138.

14. Hayes CT, et al. (2013) A new perspective on boundary scavenging in the North Pacific Ocean. *Earth and Planetary Science Letters* 369-370:86–97.
15. Yu EF, François R, Bacon MP, Fleer AP (2001) Fluxes of ^{230}Th and ^{231}Pa to the deep sea: implications for the interpretation of excess ^{230}Th and $^{231}\text{Pa}/^{230}\text{Th}$ profiles in sediments. *Earth and Planetary Science Letters* 191(3-4):219–230.
16. Black EE, Buesseler KO, Pike SM, Lam PJ (2018) ^{234}Th as a tracer of particulate export and remineralization in the southeastern tropical Pacific. *Marine Chemistry* 201:35–50.
17. Czeschel R, et al. (2011) Middepth circulation of the eastern tropical South Pacific and its link to the oxygen minimum zone. *J Geophys Res* 116(C1):1118.
18. Haskell WZ II, et al. (2015) Upwelling velocity and eddy diffusivity from ^7Be measurements used to compare vertical nutrient flux to export POC flux in the Eastern Tropical South Pacific. *Marine Chemistry* 168:140–150.
19. Steinfeldt R, Sültenfuß J, Dengler M, Fischer T, Rhein M (2015) Coastal upwelling off Peru and Mauritania inferred from helium isotope disequilibrium. *Biogeosciences* 12(24):7519–7533.
20. Kadko D (2017) Upwelling and primary production during the U.S. GEOTRACES East Pacific Zonal Transect. *Global Biogeochemical Cycles* 31(2):218–232.
21. Buesseler KO, Boyd PW (2009) Shedding light on processes that control particle export and flux attenuation in the twilight zone of the open ocean. *Limnology and oceanography* 54(4):1210–1232.
22. Ohnemus DC, et al. (2017) Elevated trace metal content of prokaryotic communities associated with marine oxygen deficient zones. *Limnology and oceanography* 62(1):3–25.